Intensified and controllable vaporization of phase-changeable nanodroplets induced by simultaneous exposure of laser and ultrasound

Qi Zhang [a,1], Yanye Yang [a,1], Honghui Xue [a,b,1], Haijun Zhang [c,d,1], Ziyan Yuan [a], Yuchen Shen [a], Xiasheng Guo [a], Zheng Fan [e], Xiaoge Wu [f,*], Dong Zhang [a,*], Juan Tu [a,*]

[a] Key Laboratory of Modern Acoustics (MOE), Department of Physics, Collaborative Innovation Center of Advanced Microstructure, Nanjing University, Nanjing 210093, China
[b] Wuxi Vocational Institute of Commerce, Wuxi 214153, Jiangsu, China
[c] Shanghai Tenth People's Hospital, School of Medicine, Tongji University, Shanghai 200092, China
[d] National United Engineering Laboratory for Biomedical Material Modification, Branden Industrial Park, Dezhou 251100, Shandong, China
[e] School of Mechanical and Aerospace Engineering, Nanyang Technological University, Singapore 639798, Singapore
[f] Environment Science and Engineering College, Yangzhou University, Yangzhou 225009, Jiangsu, China

ARTICLE INFO

ABSTRACT

Phase-changeable contrast agents have been proposed as a next-generation ultrasound contrast agent over conventional microbubbles given its stability, longer circulation time and ability to extravasate. Safe vaporization of nanodroplets (NDs) plays an essential role in the practical translation of ND applications in industry and medical therapy. In particular, the exposure parameters for initializing phase change as well as the site of phase change are concerned to be controlled. Compared to the traditional optical vaporization or acoustic droplet vaporization, this study exhibited the potential of using simultaneous, single burst laser and ultrasound incidence as a means of activating phase change of NDs to generate cavitation nuclei with reduced fluence and sound pressure. A theoretical model considering the laser heating, vapor cavity nucleation and growth was established, where qualitative agreement with experiment findings were found in terms of the trend of combined exposure parameters in order to achieve the same level of vaporization outcome. The results indicate that using single burst laser pulse and 10-cycle ultrasound might be sufficient to lower the exposure levels under FDA limit for laser skin exposure and ultrasound imaging. The combination of laser and ultrasound also provides temporal and spatial control of ND vaporization and cavitation nucleation without altering the sound field, which is beneficial for further safe and effective applications of phase-changeable NDs in medical, environmental, food processing and other industrial areas.

1. Introduction

The use of microbubbles has been well established over the past decades and its potential applications such as medical treatment [1–3], waste water treatment [4], food sterilization [5], etc. has been extensively explored [6]. As the demand for agent stability and penetration depth further increased, the substitution of microbubble gas core with superheated liquid perfluorocarbon (PFC) was proposed and the resultant agent can be made into nanoscale (usually termed as nanodroplets/nanoemulsions). Upon successful phase change, nanodroplets exhibit similar, in trend acoustic response to that of microbubbles [7]. Such phase transition is initiated acoustically, i.e., through acoustic droplet vaporization (ADV). The ADV process marks a major disadvantage for the safe application of nanodroplets as it typically requires relatively

long pulses and/or high pressures [8] that are potentially dangerous to surrounding tissues or materials. In addition, when utilizing short ADV acoustic pulses, it may be difficult to acoustically induce phase change without concomitant inertial cavitation (IC) at relatively high droplet concentrations [9]. In sight of this, it is urgent to develop one approach towards safe, controllable vaporization to reduce the sound pressure needed for initializing phase change of such agents.

On another side of phase change droplet research, it has been reported that the loading of photothermal (PTT) agents (e.g., plasmonic gold nanoparticles and dye) onto nanodroplets can effectively promote the photoacoustic (PA) effect. A possible by-product of the above-mentioned PA enhancement using PTT-loaded phase-changeable droplets is the liquid-to-gas phase transition (termed as optical vaporization) and the resulting ultrasound (US) contrast imaging capability due to the impedance mismatch between vaporized agent and surrounding environment [10]. E. Strohm *et al.* achieved successful optical vaporization of micron-sized PFC droplets loaded with silica-coated lead sulfide nanoparticles using 1064-nm laser, and the vaporization process was accompanied by PA emission [11]. K. Wilson *et al.* further showed, using gold nanorod-loaded PFC nanodroplets, that vaporization-based PA signal is much stronger than that generated from thermal expansion of plasmonic nanorods alone [12]. The laser fluence threshold values required for optical vaporization of gold nanoparticle (GNP)-loaded PFC droplets were reported to be positively related to the critical temperature of the PFC core [13]. Similar PA and following US enhancement could also be established by indocyanine green (ICG) loaded PFC nanodroplets [10]. The enhancement of PA signals was attributed mainly to joint effect of local temperature rise generated by PTT effect and the high-frequency pressure wave generated at the surface of GNPs [12]. Nevertheless, it should be pointed out that, for the phase-changeable model of opto-acoustical coupling, only the relevant research of gold nanoparticles is available, while the change of gold loaded phase change bubble has not been theoretically deduced.

Through distinct vaporization mechanisms, it is therefore of interest to explore whether optical vaporization can lower the acoustic pressure needed for the phase change of PTT-loaded droplets. Previous study on plasmonic GNPs suggests that the transient vapor bubbles formed by laser illumination can serve as nucleation sites for high-intensity focused ultrasound (HIFU)-induced cavitation, thus drastically lowering the pressure threshold for IC generation [14]. It demonstrated that the combination of time-aligned laser and US incidence enabled non-linear response generation of either GNPs [15] or GNP-coated nanoemulsions [16] at low exposure thresholds.

Building on these works, for the first time, this study investigated the light and sound exposure thresholds for GNP-loaded nanodroplets to generate long-lived (on the scale of second) bubbles that can lead to US echo enhancement or serve as cavitation nuclei. Innovatively, a comprehensive model relevant to the agent used for this study was established to describe the physical process of opto-acoustical vaporization. By introducing laser pulse into short ADV US pulses, this study aims to explore the feasibility of using localized heating effect (generated by PTT agents upon laser incidence) as a means of reducing acoustic vaporization threshold and its resultant side-effects. The results of simulation and experiment are compared, and the potential and realistic considerations for the application of opto-acoustical vaporization are discussed.

2. Theory and formulation

For theoretical derivation of the dynamics of an opto-acoustically vaporized GNP-ND, a simplified model composed of a spherical nano-droplet with a single GNP (radius R_p) located at its center was chosen to represent the geometry of GNP-ND (as is shown in Fig. 1a). This study here follows Doinikov's formulation of acoustic vaporization of PFC droplets [17], modified to incorporate Wu's formulation of a GNP subjected to acoustic and laser irradiation [18]. The model built in this
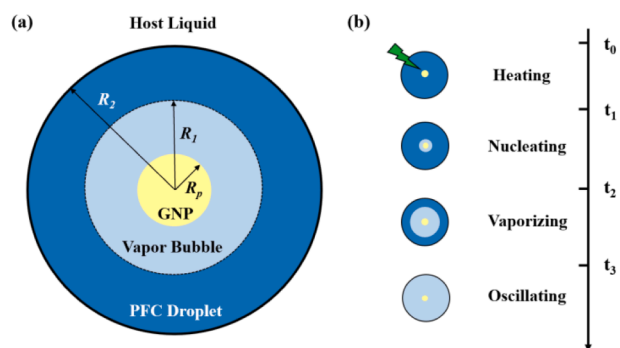

Fig. 1. (a) Schematic of the geometric model of GNP-ND. (b) Schematic and timeline of the stages of phase change modelling.

essay deduced and simulated the generation and physical quantity of the gas core through the modeling of the photothermal effect of laser on the particles. Therefore, the physical process of the opto-acoustical phase transition can be better restored from the physical point of view. The opto-acoustical vaporization of GNP-NDs is initiated by heating of GNP under laser irradiation $(t|_{t_0}^{t_1})$, followed by nucleation $(t|_{t_1}^{t_2})$, vaporization $(t|_{t_2}^{t_3})$ and finally oscillation $(t|_{t_3})$ (as is shown in Fig. 1b). Detailed description on opto-acoustical vaporization process of GNP-NDs is introduced below.

In all paragraphs below, subscripts *P*, *W*, *L* and *V* refer to GNP, water, liquid PFC and vapor PFC, respectively. The parameters that appeared in equations and their values taken are introduced and summarized in Table 1. Mathematical symbols uninvolved here are explained right after each equation.

2.1. Vaporization dynamics of droplets with pre-existing vapor bubble

For a spherical vapor bubble (radius R_1) situated at the center of a spherical PFC droplet (radius R_2), Doinikov *et al.* proposed that [17], when exposed under a sound field of pressure p_a, the evolution of vapor bubble inside the droplet can be described by Eq. (1),

Table 1
Typical material parameters used in simulations.

Parameter	Description	GNP value	Liquid PFC value	Water value
n(at 532 nm)	Number of moles	$0.41 - i \times 2.10$	1.325	1.325
k(W·m^{-1}·K^{-1})	Thermal conductivity	320	0.0556	0.60
C(J·kg^{-1}·K^{-1})	Heat capacity	128	1089.4	4200
ρ(kg·m^{-3})	Density	19.2×10^3	1590	1.0×10^3
Parameter	Description			Value
η_L(μPa·s)	Dynamic viscosity of liquid PFP			652
η_W(mPa·s)	Dynamic viscosity of water			1
m_V(kg·mol^{-1})	Molecular mass of vapor PFP			288.03×10^{-3}
C_V(J·kg^{-1}·K^{-1})	Heat capacity of vapor PFP			852.31
n_V	Number of moles of vapor PFP			1.000
L(kJ·kg^{-1})	Latent heat			116.8
σ_{12}(N·m^{-1})	Liquid/vapor PFP interfacial tension			8.54×10^3
σ_{23}(N·m^{-1})	Liquid PFP-water interfacial tension			3.5×10^3
σ_{13}(N·m^{-1})	Vapor PFP-water interfacial tension			0.07
p_0(Pa)	Atmospheric pressure			101,300
T_0(K)	Room temperature			300

Intensified and controllable vaporization of phase-changeable nanodroplets induced by simultaneous exposure of laser and ultrasound.

$$R_1 \left(\ddot{R}_1 - \frac{\dot{m}}{\rho_L 4\pi R_1^2} \right) \left[\rho_L + (\rho_W - \rho_L) \frac{R_1}{R_2} \right] + \frac{3}{2} \left(\dot{R}_1 - \frac{\dot{m}}{\rho_L 4\pi R_1^2} \right) \left\{ \dot{R}_1 \left[\rho_L \right. \right.$$

$$\left. + (\rho_W - \rho_L) \frac{R_1}{3R_2} \left(4 - \frac{R_1^3}{R_2^3} \right) \right] + \frac{\dot{m}}{2\rho_L 4\pi R_1^2} \left[\rho_L + (\rho_W - \rho_L) \frac{R_1^4}{R_2^4} \right] \right\}$$

$$= p_V - \left(\frac{\dot{m}}{4\pi R_1^2} \right)^2 \left(\frac{1}{\rho_V} - \frac{1}{\rho_L} \right) - \frac{2\sigma_{12}}{R_1} - \frac{2\sigma_{23}}{R_2}$$

$$- \frac{4}{R_1} \left(\dot{R}_1 - \frac{\dot{m}}{\rho_L 4\pi R_1^2} \right) \left[\eta_L + (\eta_W - \eta_L) \frac{R_1^3}{R_2^3} \right] - p_0 - p_a, \tag{1}$$

Where dots denote time derivative, m the mass flux through the vapor bubble surface, p_V the pressure within the vapor bubble, p_0 the atmospheric pressure, p_a the acoustic pressure, ρ_L the density of liquid PFC and ρ_W the density of water, σ_{12} the surface tension at the vapor–liquid PFC interface, σ_{23} the surface tension at the liquid PFC-water interface, η_L the dynamic viscosity of liquid PFC and η_W the dynamic viscosity of water.

The size of vapor bubble and PFC droplet is further restricted by mass conservation at their interface, which can be written as

$$\dot{R}_2 = \frac{R_1^2}{R_2^2} \left(\dot{R}_1 - \frac{\dot{m}}{\rho_L 4\pi R_1^2} \right), \tag{2}$$

Meanwhile, under the assumption of spatially uniform temperature field within the vapor bubble, the heat transfer between vapor bubble and PFC droplet gives the following equations

$$\rho_V = \frac{p_V}{R_{gV} T_V}, \tag{3}$$

$$\dot{m} = \frac{k_L}{L} 4\pi R_1^2 \frac{\partial T_L}{\partial r} \bigg|_{r=R_1}, \tag{4}$$

$$\frac{\partial T_L}{\partial t} + v_L \frac{\partial T_L}{\partial r} - \frac{1}{r^2} \frac{\partial}{\partial r} \left(D_L r^2 \frac{\partial T_L}{\partial r} \right) = \frac{12\eta_L}{\rho_L c_L} \frac{v_L^2}{r^2}, \tag{5}$$

$$\frac{\partial T_W}{\partial t} + v_W \frac{\partial T_W}{\partial r} - \frac{1}{r^2} \frac{\partial}{\partial r} \left(D_W r^2 \frac{\partial T_W}{\partial r} \right) = \frac{12\eta_W}{\rho_W c_W} \frac{v_W^2}{r^2}, \tag{6}$$

where $R_{gV} = R_g/m_V$ stands for the gas constant of vapor, R_g is the universal gas constant and m_V is the molecular weight of the vapor. $D_i = k_i/(\rho_i C_i), i = L, W$ is the thermal diffusivity (unit $\mathrm{m^2 \cdot s^{-1}}$). T means the temperature (unit K), v means the vibration velocity (unit m/s), c means the sound velocity (unit m/s). The boundary conditions of Eq. (6) are given by

$$T_W|_{r\to\infty} = T_0, \tag{7}$$

$$T_L|_{r=R_2} = T_W|_{r=R_2}, \tag{8}$$

$$T_L|_{r=R_1} = T_V. \tag{9}$$

2.2. Opto-acoustical vapor bubble nucleation dynamics

For the case of this study, the initial conditions for the above-described vaporization process ($t|_{t_2}^{t_3}$) are determined by previous heating ($t|_{t_0}^{t_1}$) and nucleation ($t|_{t_1}^{t_2}$) process. As nanosecond-duration single laser shot and microsecond-duration tone-burst US were used to vaporize the droplet, the acoustic pressure can be regarded as constant during laser incidence. The temperature of GNP during laser-induced heating ($t|_{t_0}^{t_1}$) can be expressed by

$$C_P m_P \frac{\partial T_P}{\partial t} = Q - 4\pi R_P^2 \left(-k_L \frac{\partial T_L}{\partial r} \bigg|_{r=R_P} \right), \tag{10}$$

where C_P, m_P, T_P, R_P are the heat capacity, mass, temperature and radius of GNP, respectively. k_L is the thermal conductivity of the liquid

PFC. Q represents the absorption power that equals to the rate of heat generation of GNP and can be calculated by $Q = Q_{abs}\pi R_P^2 I_0$, where Q_{abs} is the absorption coefficient that acquired using Mie analysis and I_0 the intensity of laser pulse (unit $\mathrm{W \cdot m^{-2}}$). For area outside the GNP, thermal conduction gives

$$\frac{\partial T_i}{\partial t} = \frac{1}{r^2} \frac{\partial}{\partial r} \left(D_i r^2 \frac{\partial T_L}{\partial r} \right), i = L, W, \tag{11}$$

where the initial condition of temperature is $T_i = T_0, i = P, L, W$, with T_0 being the ambient temperature. The temperature field boundary condition is $T_W|_{r\to\infty} = T_0$ and temperature continuity at the particle-liquid PFC, and liquid PFC-water interface.

The heating ($t|_{t_0}^{t_1}$) process ends and nucleation ($t|_{t_1}^{t_2}$) takes over when the spatial average temperature within a thin layer (thickness being δ_L) of liquid PFC exceeds vaporization temperature T_{vp}. The value of δ_L is determined such that, once vaporized, the conservation of mass gives the thickness of vapor blanket δ_V formed to due vaporization equals the length of mean free path λ of vapor molecule

$$\delta_V = \lambda = \frac{k_B T_{vp}}{\sqrt{2}\pi d^2 p_{vp}}. \tag{12}$$

Here, k_B is the Boltzmann constant and T_{vp} and p_{vp} are the temperature and local pressure at which the temperature initiates, which are further related through Clapeyron-Clausius equation as well as pressure continuity at the vapor blanket-liquid PFC interface $p_{vp} = p_0 + \frac{2\sigma(T_{vp})}{R_p} + p_a\sin\varphi.\sigma(T_{vp})$ is the surface tension at temperature T_{vp}, and $p_a\sin\varphi$ stands for the imposed ultrasound field.

In the course of nucleation, the size of vapor blanket evolves under the combined influence of pressure differences at the vapor–liquid interface and evaporation of liquid PFC

$$\dot{R}_1 = u + \frac{\dot{m}}{\rho_L 4\pi R_1^2} \frac{\rho_L}{\rho_V}. \tag{13}$$

In Eq. (13), the first term u denotes the contribution of the Laplace pressure and can be found from

$$\frac{1}{2}m_{\mathrm{eff}}u^2 = \int_{R_P}^{R_1} p_{\mathrm{exc}} 4\pi r^2 dr = \int_{R_P}^{R_1} \left(\frac{2\sigma_1}{R_P} - \frac{2\sigma_1}{r} \right) 4\pi r^2 dr, \tag{14}$$

where m_{eff} is the effective mass of liquid surrounding the vapor bubble (unit kg). The second term describes the contribution of ongoing evaporation, where $\dot{m}$ stands for mass flux and can be determined from the law of energy conservation

$$\dot{m}L = 4\pi R_P^2 \left(-k_V \frac{\partial T_V}{\partial r} \right) \approx 4\pi R_P^2 \left(-k_V \frac{T_V|_{r=R_1} - T_P}{R_1 - R_P} \right), \tag{15}$$

L here is the latent heat and k_V is the thermal conductivity of vapor PFC. Nucleation process ends at $t = t_2$ when the thickness of vapor bubble grows to the mean free path of vapor

$$R_1|_{t=t_2} = R_P + \delta_V, \tag{16}$$

And values at that time point set the initial conditions for the vaporization process are described in above sections.

2.3. Numerical calculation methods

Generally, the mathematical model built above contains ordinary differential equations (ODE) which is time dependent, and partial differential equations (PDE) which is time as well as space dependent. Since the interface of vapor and liquid is mobile, traditional finite difference method or finite element method will face the problem of low precision. Here, the Chebyshev spectral collocation method [19] was used as a solution. With the Chebyshev-Lobatto interpolation method, PDEs can be converted to ODEs, and then solved by the traditional finite difference method using MATLAB$^{\mathrm{TM}}$ (The MathWorks, MA).

3. Materials and methods

3.1. Nanodroplet preparation and characterization

DSPC, DPPG and DSPE-PEG-2000 (850365P, 880120P and 840455P respectively, Avanti Polar Lipids, Inc., USA) were dispersed with molecular ratio of 36:4:9 in 2:1 v/v chloroform and methanol solvent, which was later removed by rotary evaporation. The resultant lipid film was then rehydrated (1 mg/ml) and 10 ml of the rehydrated liquid solution was co-incubated under stirring with 2.5 mg/ml polyvinyl pyrrolidone (PVP, R0508, NJDuly Inc., China) and 2.5 ml GNP solution (0.04 mg/ml, Xi'an Ruixi Biological Technology Co., China) for 2 h. Following incubation, the mixture was centrifuged (3000 rpm, 5 min) to remove excess, unbounded PVP and GNP. The sediment after centrifuge was resuspended using deionized water (1 mg/ml). Finally, 800 μl PFP was added to 10 ml of the resuspended solution and sonicated together for 20 s under ice bath using an ultrasonic processor (VCX 750, Vibra-Cell Processors, Sonic & Materials, Inc., CT) at 30 % output setting (20 kHz, 225 W output power approx.). The droplets were collected by centrifuge at 1000 rpm for 5 mins and were stored at 4 ℃.

As shown in Fig. 2, the successful loading of GNP on NDs was confirmed through transmission electron microscopy (TEM). Fig. 2 illustrates that, with the assessment of a spectrometer (Cary 50, Agilent, USA), the absorption spectrum of GNP-ND sample exhibits a peak that corresponds to the absorption peak of GNP sample (at around 532 nm). The GNP-NDs were tested for size distribution using a dynamic-light-scattering-based particle sizer (Nanobrook 90 Plus Zeta; sizing range: 0.3 nm-6 μm; Brookhaven Instruments, USA), and microscope-examined for concentration. Fig. 3 shows the size distribution of synthesized GNP-NDs and blank NDs (fabricated with the same procedure without GNPs), the average hydrodynamic diameter of which are 538.02 nm and 397.08 nm respectively. To avoid the problems of insufficient nuclei or interactions between droplets reported in the previous work [9], synthesized droplets were pipette-diluted with deionized water to designated concentration of 5×10^6/ml before experiment, and the remaining was stored in a refrigerator at 4 ℃.

3.2. Experimental setup

Fig. 4 illustrates the diagram of experimental apparatus. This study employed a Q-switched Nd:Yag laser (Surelite I-10[TM], Continuum, USA) operating at 532 nm wavelength and a time-aligned 1.1-MHz focused US transducer (custom-made, 70 mm geometric diameter, −6 dB focal volume = 15.99 mm^3). All experiments were conducted in a water tank filled with room-temperature, degassed, filtered water, the dissolved oxygen (DO) level of which was monitored to be lower than 3 ppm using a DO meter (9010 M, Jenco Inc., USA). The laser pulse possessed a nominal pulse width of 5-ns and beam diameter of 6 mm, and its output energy was measured a power meter (Labmax-Top, Coherent Inc., USA). Fluence value reported in this study considered the light attenuation

through 10 cm of water (distance between the glass optical window and the acoustic focus). The custom-made transducer had a glass-sealed hole at its geometric center, enabling the laser beam to pass through with minimal transmission loss and be aligned co-axially. For all measurement, the focused transducer was driven by 1.1 MHz, 10-cycle sine bursts, which were generated by a waveform generator (33600 A, Agilent Technologies, USA), passed through a 53-dB power amplifier (2200 L, Electronics and Innovation, Ltd., USA) and an impedance matching box, then sent to the excitation transducer. The acoustic pressure field, including focal volume and focal sound pressure, was measured using a needle hydrophone (S/N 328, Chinese Academy of Sciences, China), which was recently calibrated before measurement using reciprocity method over the frequency range of 1–15 MHz to ensure its performance.

The timing between acoustic and laser pulse was adjusted such that the acoustic focal area subjected to simultaneous acoustic and laser exposure [14–16,20]. A metal target and the above-mentioned needle hydrophone was employed for this time alignment purpose. The target was placed roughly at the focus of the acoustic transducer and the hydrophone was oriented perpendicular to the acoustic beam focus. The position of the target and hydrophone was first adjusted using 3-D positioning stage for acoustic alignment by maximizing the scattered acoustic signal of the target. Then, the trigger-and-delay system was built by using the laser sync out as an input trigger for the waveform generator, and delay was achieved through built-in delay function of the waveform generator. If properly time-aligned, the PA signal of the target (laser only) should fall into the same time period where scattered acoustic signal (US only) reached the hydrophone. Due to a higher travel speed of light than sound, this trigger-and-delay design inevitably results in missing the first laser shot (within a sequence of repeated laser shots). Thus, the delay of waveform generator was adjusted so that acoustic wave arrives one burst period later than the laser pulse. To allow possible jittering of the system, the PA signal was matched to the third cycle of scattered acoustic signal. The target and hydrophone were removed after the alignment.

For phase change measurement, a dialysis tubing (6 mm diameter, MEMBRACEL®, Viskase® Companies, Inc., IL) was placed at the focus of acoustic transducer, and a syringe pump (Legato 270, KD Scientific Inc., MA) was employed to push the samples through the dialysis tube at a constant volume velocity (150 μl/s) so as to guarantee fresh, unexposed samples for every light and sound exposure in the time period of $\Delta T = 5$ s. To quantitively evaluate the degree of phase change, a 7.5-MHz linear-array imaging probe was positioned to interrogate regions approximately 1.2 cm downstream the transducer focal volume. The distance between the B-mode imaging plane and the acoustic focus of excitation transducer was selected such that only vaporization-generated bubbles that had survived approximately 1 s, which were of high clinical significance [21], were imaged. B-mode images were acquired by a commercial US imaging system (MI < 0.4, Terason t3000[TM], Teratech, MA), stored at a frame rate of 10 Hz, and processed offline using MATLAB[TM]
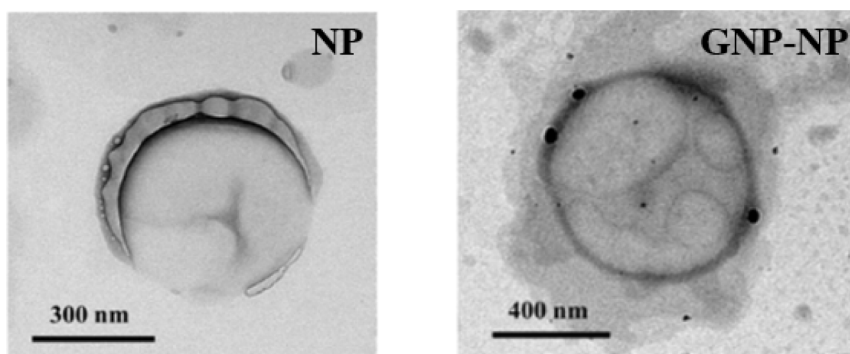

Fig. 2. Representative Transmission electron microscopy (TEM) images of blank nanodroplets (NDs) and gold nanoparticle-loaded nanodroplets (GNP-NDs).
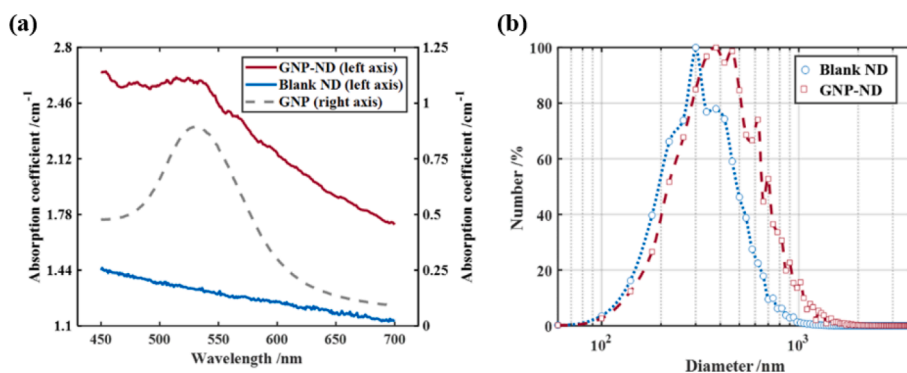
Fig. 3. (a) Wavelength-dependent absorption coefficient of gold nanoparticles (GNPs, right axis), blank NDs (left axis) and GNP-NDs (left axis). (b) Size distribution of blank NDs and GNP-NDs.
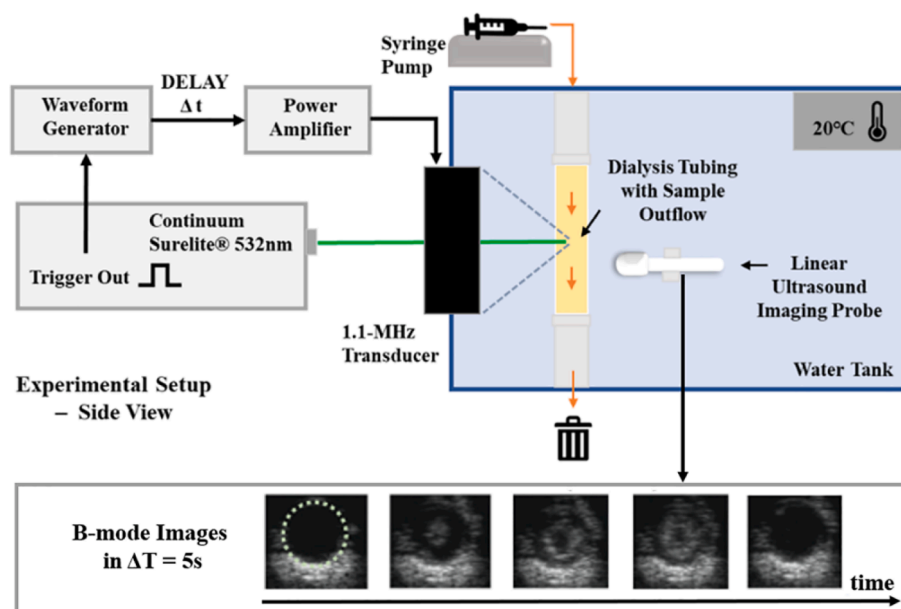

Fig. 4. Illustration of experiment setup for the initiation of opto-acoustical vaporization and the determination of mean echo enhancement of vaporized droplets (dotted circle – the region of interest).

(The MathWorks, MA). Representative B-mode images in $\Delta T = 5$ s were demonstrated in Fig. 4, while dotted circle represented the region of interest (ROI) defined by the walls of dialysis tubing. It can be clearly seen that the phase-changed droplets moved from the focus area of the transducer to the detection area of the B-mode transducer (the first 4 images), and were completely discharged from the detection area within 5 s (the last image). This indicates that the current flow rate of 150 µl/s can ensure that the measurement results between different exposures are independent of each other and not affected.
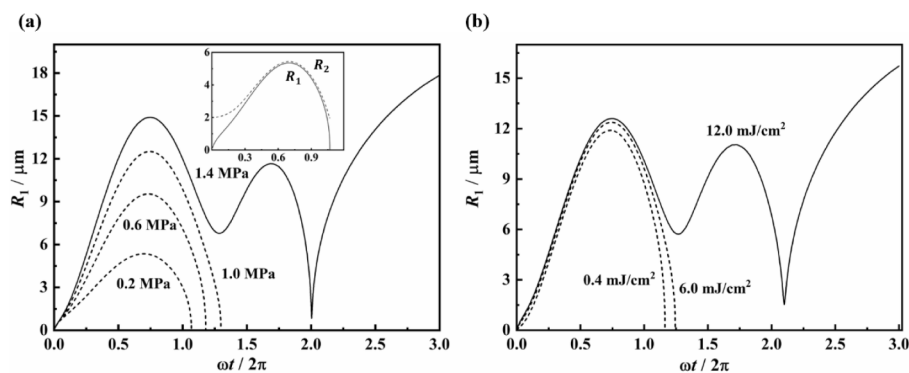
3.3. Data processing

Similar to previous work [9], the mean echo enhancement (MEE) of gray scale B-mode images was chosen as the phase change indicator. For each frame acquired, the average gray scale brightness value within ROI were calculated and defined as mean echo level (MEL). Background MEL (liquid droplets) was established by averaging B-mode frames acquired immediately preceding the light and sound exposure. For every desired exposure pair in terms of laser fluence and sound pressure, 40 independent recordings were performed and repetition rate of exposures was limited to 0.2 Hz to ensure bubble-free steady-state before every exposure. Note that for all exposure pair, recording started at the second laser pulse as the acoustic wave was delayed to meet the second laser pulse.

After subtracting background MEL, the MEE for a particular exposure pair is then determined by averaging over 40 repeated measurements.

4. Results

4.1. Simulated results

The model established in this study gives the radial evolution $(R - t)$ of vapor and liquid PFC bubble upon laser and US incidence. Fig. 5 plots the $R - t$ curve of vapor bubble (R_1) formed under (a) 10 mJ/cm^2 fluence accompanied by 0.2, 0.6, 1.0 and 1.4 MPa peak negative US pressure; (b) 1 MPa peak negative US pressure accompanied by 0.4, 6.0 and 12 mJ/cm^2 fluence. As can be found from Fig. 5a, the maximum radius (R_{max}) as well as the life span of vapor cavity increases with increasing US pressure. For pressures below 1.4 MPa, the vapor cavity vanished after its first expansion period, indicating a typical "unsuccessful" phase change. Note that for a "unsuccessful" phase change, the size of vapor bubble is always smaller than that of liquid PFC $(R_1 < R_2$, see inset of 4a). When the US pressure became high enough (e.g. $p_- = 1.4$ MPa), the condition $R_1 = R_2$ can be satisfied during vaporization process $(t|_{t_2}^{t_3})$ and thus the fully vaporized GNP-ND continues to oscillate under the following US wave.

Fig. 5. Simulation results of radius evolution of GNP-NDs subjected to opto-acoustical vaporization of various parameters, (a) 10 mJ/cm² laser together with 0.2 MPa, 0.6 MPa, 1.0 MPa and 1.4 MPa ultrasound, with the inset showing the radius evolution of the vapor bubble (R_1) and that of the droplet (R_2); (b) 1 MPa ultrasound together with 0.4 mJ/cm², 6.0 mJ/cm² and 12.0 mJ/cm² laser. The dashed lines indicate "unsuccessful" phase change and solid lines indicate "successful" phase change (the inset excluded).

Similar $R-t$ curve of vapor bubble (R_1) can be witnessed in Fig. 5b, where fluence smaller than 12 mJ/cm² (viz., 0.4 and 6.0 mJ/cm²) was demonstrated insufficient in generating complete phase change (when accompanied by US sonication of $p_- = 1$ MPa). However, it is interesting to see that for "unsuccessful" phase change, varying the fluence (Fig. 5b) does not result in as obvious variation in R_{max} as that caused by varying the US pressure (Fig. 5a). This can be explained by rethinking the role of ultrasound and laser in the whole GNP-ND phase change process – heating from the laser initiates the nucleation of a vapor blanket, after which the dynamics of vapor bubble becomes dominated by US sonication. Thus, it is reasonable to find that R_{max} is more sensitive to changes in US pressure rather than laser fluence.

4.2. Experimental results

This study investigated GNP-ND phase change behavior under 4 difference laser fluence (0 mJ/cm², 16.9 mJ/cm², 116.5 mJ/cm² and 305.9 mJ/cm²) and 12 different sound pressures (ranging from 0 MPa to 7.56 MPa). As is shown in Fig. 6, the MEE of GNP-ND increases with increasing sound pressure at different rates – the higher the laser fluence, the faster the rate. The MEE tends to saturate as sound pressure further rises, which could be attributed to quicker bubble collapse and in line with the previous work [22]. The relationship between MEE and sound pressure can be quantitively described by fitting the MEE curve (MEE values acquired at the same laser fluence as a function of sound pressure) to a sigmoid function that took form of

$$y = max_{(y)} + \frac{min_{(y)} - max_{(y)}}{1 + (x/a)^b}, \tag{15}$$

where $max_{(y)}$ and $min_{(y)}$ are the maximum and minimum value within one MEE curve. By further fitting two lines respectively to the flat and uprising portion of sigmoid, their intersection can be taken as the threshold value of phase change. The US threshold for phase change dropped dramatically as laser was employed (the pressure threshold $p_t = 6.2$ MPa for fluence $= 0$ mJ/cm² and $p_t = 0.0646$ MPa for fluence $= 16.9$ mJ/cm²). This decrease in US threshold significantly slowed down as the fluence further rises ($p_t = 0.0315$ MPa for fluence $= 116.5$ mJ/cm² and $p_t = 5.19 \times 10^{-4}$ MPa for fluence $= 305.9$ mJ/cm²). These results show that the involvement of a certain level of laser fluence (as low as 16.9 mJ/cm²) can effectively reduce the US threshold for GNP-ND phase change by several orders of magnitude. It should be noted that such effect is much less obvious as fluence further increases.

4.3. Comparison between simulated and experimental results

The simulation and experiment conducted in this study approaches the vaporization problem of GNP-NDs from two different perspectives and therefore cannot be quantitively compared. The simulated results provide a description on single droplet vaporization while experimental results provide quantitative information on the ensemble average of droplets distributed throughout the HIFU focus and the laser beam path. The comparison is thus established by analyzing the laser fluence and US pressure exposure pair that enables the same levels of phase change.

For the formulated model, a series of exposure pair threshold values under which the droplet satisfies $R_1 = R_2$ during the vaporization process ($t|_{t_2}^{t_3}$) can be acquired. Such exposure pair threshold values are herein referred to as equal-effect exposure pairs in terms of inducing the same degree of phase change and is shown in Fig. 7a. These equal-effect exposure pairs form an equal-effect curve (EEC) for the selected MEE value. For a more intuitive comparison, these simulated results were fitted as an exponential function $y = Ae^{Bx}$, while y represented pulse energy of laser, x represented peak negative pressure of ultrasound. According to the simulated results, the coefficients would be A = 445400 and B = -10.07 (coefficient of regression $R^2 = 0.9972$).

For experiment results, a summary of equal-effect light and sound exposure pairs in terms of achieving the same MEE can be found in Fig. 7b. The MEE value to be explored was set to be 28.28a.u., which corresponds to the MEE achieved by ADV only under 7.56 MPa sound pressure. Qualitative agreement can be found between the EEC of the formulated model and experiment results, where the US pressure required for phase change declines exponentially with the fluence used. This marks an important feature of opto-acoustical vaporization that compared with ultrasound, laser became much less significant above certain fluence.
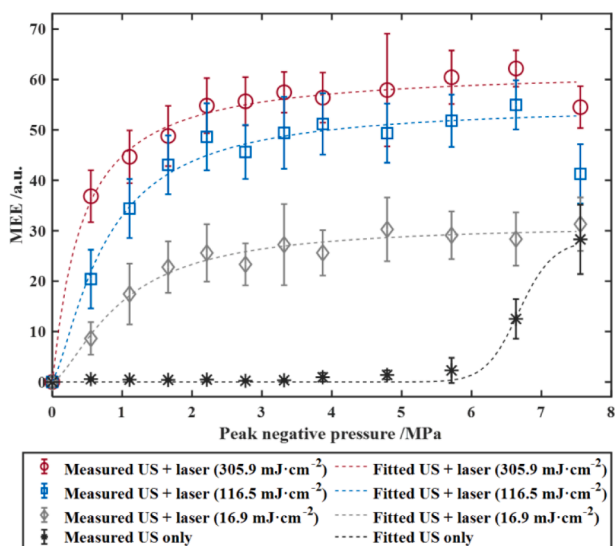

Fig. 6. Mean echo enhancement produced by opto-acoustically vaporized GNP-NDs under different laser fluence and sound pressures.
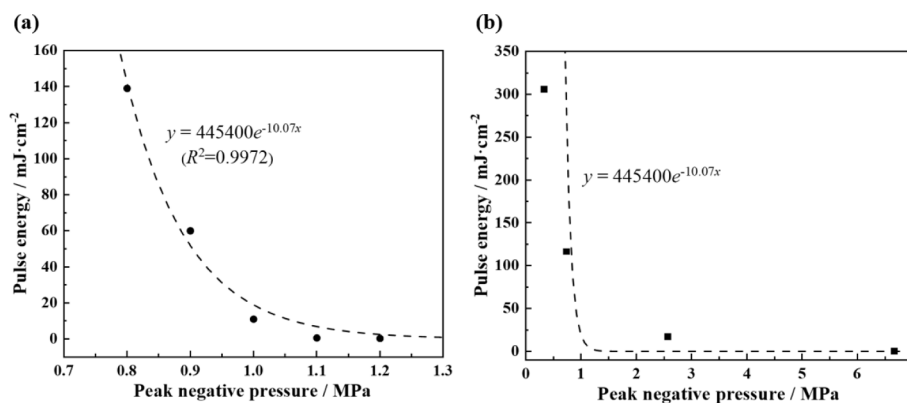
Fig. 7. (a) Simulated results and the equal-effect curve (EEC) acquired from the simulation (fitted using exponential function). (b) Experimental results and the comparison with the simulated EEC.

5. Discussion

It was shown in an earlier study that [9], for droplets undergoing US-induced phase change, increasing the concentration of droplets can result in an increase of saturated MEE (maximum value achieved within one MEE curve). Interestingly, the incorporation of laser in the phase change process was observed to achieve similar effects (saturated MEE increased from 28.28 a.u. to 62.19 a.u. as the fluence rose from 0 mJ/cm^2 to 305.9 mJ/cm^2). This effect is mainly attributed to the additional laser heating effect during nucleation, where an initial vapor blanket is formed for subsequent vaporization. The formation of such vapor blanket provides initial velocity for its further evolvement under combined influence of US field, PFP evaporation and interfacial tension. For this experiment where droplet group response is concerned, the contribution of laser enables phase change of smaller droplets which would otherwise fail to vaporize under sole influence of US. This MEE-boosting effect of laser employment thus suggest another approach towards US imaging enhancement other than increasing droplet concentration.

From the EECs shown in Fig. 7, it can be seen that combining laser and ultrasound induces phase change of GNP-NDs much more efficiently than using solely/primarily light or sound. As the fitted curve approaches either axis, the threshold for vaporization gradually approximates the scenario of either ADV or optical vaporization, both of which have been criticized for their high level of exposure energy and the concomitant side-effects. In this study, there was no measurable phase change for GNP-NDs exposed only to laser, even under the highest laser fluence (305.9 mJ/cm^2) used. It was also above at least 5.71 MPa when the enhancement of contrast by GNP-NDs post-ADV was observed. However, when laser and ultrasound are combined, the exposure can be downscaled below the maximum permissive exposure for skin (20 mJ/cm^2 for pulsed laser at 532 nm (ANSI LIA LASER Z136.1-2014)) as well as mechanical index (MI) Food and Drug Administration (FDA) limitation for ultrasound imaging (1.9, corresponds to 1.99 MPa at 1.1 MHz). This suggest that the combination of laser and ultrasound irradiation may be a possible solution towards safe vaporization of NDs. As this study explored opto-acoustically vaporized NDs with lifetime on the scale of one second, these sustained vaporized NDs can further act as either US contrast agents for imaging purposes or cavitation nucleus for treatment purposes. The feasibility of integrating diagnostic and therapeutic purposes by designing specific US sequences has been verified in an earlier study on acoustically vaporized NDs [23], and could be adapted to opto-acoustically vaporized NDs with minimal change.

This study selected GNPs to act as the PTT agent due to its photostability and feasibility of modelling. The durability of GNPs is beneficial in terms of enabling long-term tracking of target sites as well as repeated nucleation. When it comes to practice (especially to clinical use), however, the involvement of nanoparticles remains controversial and

requires extensive safety evaluation [24]. Several improvements can be made to pave the way of the application of opto-acoustical vaporization and light-sound sensitive agents. First, surface chemistry, ligands and physiological properties of nanoparticles can be adjusted to lower their cytotoxicity [25] and lower their nonspecific accumulation in the mononuclear phagocyte system [26]. It is also possible to make use of clinically approved dye with PTT nature (such as ICG [10,26]) as a substitution. Second, the resonance frequency of PTT agents can be tailored to match the near-infrared 'optical window' of biological tissues where the penetration depth of light is lengthened [27] and the maximum permissive exposure (MPE) increases (20 mJ/cm^2 at 532 nm, 32.89 mJ/cm^2 at 808 nm and 100 mJ/cm^2 at 1050 nm-1400 nm; ANSI LIA LASER Z136.1-2014). Third, as was observed on this study (and in accordance with other established studies on photoacoustic cavitation [16,18]), the localized heating effect contributed by laser towards acoustic cavitation signal generation/phase change only remains significant below certain exposure level. In other words, by mapping the laser and US exposure parameters as well as the quantity of PTT agents loading, an optimal exposure combination with minimal nanoparticle dosage could be determined under the trade-off between vaporization efficacy and physiological side-effects.

6. Conclusion

This study explored the potential of generating long-lived (on the scale of a second) vaporization bubbles using simultaneous laser and ultrasound short pulses of reduced exposure parameters. Gold-loaded nanoscale droplets were selected as a representative of dual-modal light/sound responsive agents. A theoretical model was established to explore and describe the physical process of NDs undergoing opto-acoustical vaporization. The phase change outcome, featured by enhanced ultrasound echo signals, were quantitively assessed under various exposure parameters (4 difference laser fluence: 0, 16.9, 116.5 and 305.9 mJ/cm^2 and 12 different sound pressures ranging from 0 to 7.56 MPa). The simulation predictions and experiment results shared qualitative agreement, showing that the combination of simultaneous, single burst laser pulse and 10-cycle ultrasound pulse effectively reduce the exposure threshold of vaporizing GNP-NDs compared to using solely/primarily-one mechanism of vaporization (either optical vaporization or ADV). It was suggested that, for opto-acoustical vaporization, synthesized GNP-NDs only require the laser fluence below MPE limit and the ultrasound pressure below imaging MI limit. Thus, opto-acoustical vaporization can achieve precise temporal and spatial control of the generation of bubbles by merely controlling the laser flash, as only where light and sound coincides is the phase change possible. By generating spatially controlled cavitation under modest ultrasound field, it is expected that bubbles generated from opto-acoustical vaporization can be further exploited for practical application purposes in the

fields of industry, medicine, food processing and environmental engineering, etc.

Declaration of Competing Interest

The authors declare that they have no known competing financial interests or personal relationships that could have appeared to influence the work reported in this paper.

Data availability

No data was used for the research described in the article.

Acknowledgements

References

[1] R. Song, C. Zhang, F. Teng, J. Tu, X. Guo, Z. Fan, Y. Zheng, D. Zhang, Cavitation-facilitated transmembrane permeability enhancement induced by acoustically vaporized nanodroplets, Ultra. Sonochem. 79 (2021) 105790.

[2] B.Z. Fite, J. Wang, P. Ghanouni, K.W. Ferrara, A review of imaging methods to assess ultrasound-mediated ablation, BME Front. 2022 (2022) 9758652. https://doi.org/10.34133/2022/9758652.

[3] C. Childers, C. Edsall, I. Mehochko, W. Mustafa, Y.Y. Durmaz, A.L. Klibanov, J. Rao, E. Vlaisavljevich, Particle-mediated histotripsy for the targeted treatment of intraluminal biofilms in catheter-based medical devices, BME Front. 2022 (2022) 9826279. https://doi.org/10.34133/2022/9826279.

[4] H. Zhang, B. Wang, C. Gao, T. Zhu, M. Xiong, H. Ren, Effective degradation of hydrolyzed polyacryamide (HPAM) in a simultaneous combination of acoustic cavitation and microbubbles ozonation: Process optimization and degradation mechanism, Process Saf. Environ. 159 (2022) 465–476, https://doi.org/10.1016/j.psep.2022.01.007.

[5] M.P. Walsh, R.V. Tikekar, N. Nitin, S. Wrenn, Phospholipid bilayer responses to ultrasound-induced microbubble cavitation phenomena, J. Food. Eng. 294 (2021), 110410, https://doi.org/10.1016/j.jfoodeng.2020.110410.

[6] Y. Yang, Q. Li, X. Guo, J. Tu, D. Zhang, Mechanisms underlying sonoporation: Interaction between microbubbles and cells, Ultra. Sonochem. 67 (2020), 105096. https://doi.org/ 10.1016/j.ultsonch.2020.105096.

[7] J. Tu, A.C.H. Yu, Ultrasound-mediated drug delivery: sonoporation mechanisms, biophysics, and critical factors, BME Front. 2022 (2022) 9807347. https://doi.org/10.34133/2022/9807347.

[8] E. Stride, T. Segers, G. Lajoinie, S. Cherkaoui, T. Bettinger, M. Versluis, M. Borden, Microbubble agents: new directions, Ultra. Med. Biol. 46 (2020) 1326–1343, https://doi.org/10.1016/j.ultrasmedbio.2020.01.027.

[9] Y. Yang, D. Yang, Q.i. Zhang, X. Guo, J.L. Raymond, R.A. Roy, D. Zhang, J. Tu, The influence of droplet concentration on phase change and inertial cavitation thresholds associated with acoustic droplet vaporization, J. Acoust. Soc. Am. 148 (4) (2020) EL375–EL381.

[10] A. Hannah, G. Luke, K. Wilson, K. Homan, S. Emelianov, Indocyanine Green-Loaded Photoacoustic Nanodroplets: Dual Contrast Nanoconstructs for Enhanced Photoacoustic and Ultrasound Imaging, ACS Nano 8 (2014) 250–259, https://doi.org/10.1021/nn403527r.

[11] E. Strohm, M. Rui, I. Gorelikov, N. Matsuura, M. Kolios, Vaporization of perfluorocarbon droplets using optical irradiation, Biomed, Opt. Express 2 (2011) 1432–1442, https://doi.org/10.1364/BOE.2.001432.

[12] K. Wilson, K. Homan, S. Emelianov, Biomedical photoacoustics beyond thermal expansion using triggered nanodroplet vaporization for contrast-enhanced imaging, Nat. Commun. 3 (2012) 618, https://doi.org/10.1038/ncomms1627.

[13] J.D. Dove, P.A. Mountford, T.W. Murray, M.A. Borden, Engineering optically triggered droplets for photoacoustic imaging and therapy, Biomed, Opt. Express 5 (2014) 4417–4427, https://doi.org/10.1364/BOE.5.004417.

[14] C.H. Farny, T. Wu, R.G. Holt, T.W. Murray, R.A. Roy, Nucleating cavitation from laser-illuminated nano-particles, Acoust. Res. Lett. Onl. 6 (2005) 138–143, https://doi.org/10.1121/1.1897823.

[15] J.R. McLaughlan, R.A. Roy, H. Ju, T.W. Murray, Ultrasonic enhancement of photoacoustic emissions by nanoparticle-targeted cavitation, Opt. Lett. 35 (2010) 2127–2129. https://doi.org/10.1364/OL.35.002127.

[16] B. Arnal, C. Perez, C.-W. Wei, J. Xia, M. Lombardo, I. Pelivanov, T.J. Matula, L. D. Pozzo, M. O'Donnell, Sono-photoacoustic imaging of gold nanoemulsions: Part I. Exposure thresholds, Photoacoustics 3 (2015) 3–10, https://doi.org/10.1016/j.pacs.2014.12.001.

[17] A.A. Doinikov, P.S. Sheeran, A. Bouakaz, P.A. Dayton, Vaporization dynamics of volatile perfluorocarbon droplets: A theoretical model and in vitro validation, Med. Phys. 41 (10) (2014) 102901.

[18] T. Wu, C.H. Farny, R.A. Roy, R.G. Holt, Modeling cavitation nucleation from laser-illuminated nanoparticles subjected to acoustic stress, J. Acoust. Soc. Am. 130 (2011) 3252–3263, https://doi.org/10.1121/1.3626133.

[19] Y. Hao, A. Prosperetti, The dynamics of vapor bubbles in acoustic pressure fields, Phys. Fluids 11 (1999) 2008–2019, https://doi.org/10.1063/1.870064.

[20] H. Ju, R.A. Roy, T.W. Murray, Gold nanoparticle targeted photoacoustic cavitation for potential deep tissue imaging and therapy, Biomed, Opt. Express 4 (2013) 66–76. https://doi.org/10.1364/BOE.4.000066.

[21] N. Rezinik, R. Williams, P.N. Burns, Investigation of Vaporized Submicron Perfluorocarbon Droplets as an Ultrasound Contrast Agent, Ultrasound Med. Biol. 37 (2011) 1271–1279, https://doi.org/10.1016/j.ultrasmedbio.2011.05.001.

[22] H. Xu, J. Tu, F. Niu, P. Yang, Cavitation dose in an ultrasonic cleaner and its dependence on experimental parameters, Appl. Acoust. 101 (2016) 179–184, https://doi.org/10.1016/j.apacoust.2015.08.020.

[23] K.-I. Kawabata, R. Asami, H. Yoshikawa, T. Azuma, S.-I. Umemura, Sustaining Microbubbles Derived from Phase Change Nanodroplet by Low-Amplitude Ultrasound Exposure, Jpn. J. Appl. Phys. 49 (2010) 07HF20, https://doi.org/10.1143/JJAP.49.07HF20.

[24] N. Lewinski, V. Colvin, R. Drezek, Cytotoxicity of nanoparticles, Small 4 (1) (2008) 26–49.

[25] M. Bhamidipati, L. Fabris, Multiparametric Assessment of Gold Nanoparticle Cytotoxicity in Cancerous and Healthy Cells: The Role of Size, Shape, and Surface Chemistry, Bioconjugate Chem. 28 (2016) 449–460, https://doi.org/10.1021/acs.bioconjchem.6b00605.

[26] X. Jiang, B. Du, Y. Huang, M. Yu, J. Zheng, Cancer Photothermal Therapy with ICG-conjugated Gold Nanoclusters, Bioconjugate Chem. 31 (2020) 1522–1528, https://doi.org/10.1021/acs.bioconjchem.0c00172.

[27] A.N. Bashkatov, E.A. Genina, V.I. Kochubey, V.V. Tuchin, Optical properties of human skin, subcutaneous and mucous tissues in the wavelength range from 400 to 2000nm, J. Phys. D: Appl. Phys. 38 (2005) 2543–2555, https://doi.org/10.1088/0022-3727/38/15/004.